

# TURBULENT DISPERSION OF PARTICLES IN THE WAKE OF A MOVING VEHICLE

MANISH KUMAR



DEPARTMENT OF APPLIED MECHANICS

INDIAN INSTITUTE OF TECHNOLOGY DELHI

FEBRUARY 2026

© Indian Institute of Technology Delhi (IITD), New Delhi, 2026

# TURBULENT DISPERSION OF PARTICLES IN THE WAKE OF A MOVING VEHICLE

by

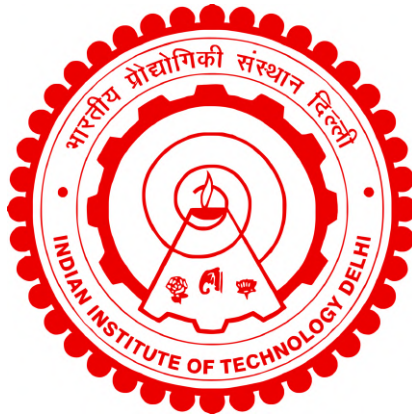
MANISH KUMAR

DEPARTMENT OF APPLIED MECHANICS

Submitted

in fulfilment of requirements for the degree of Doctor of Philosophy

to the



INDIAN INSTITUTE OF TECHNOLOGY DELHI

FEBRUARY 2026

*Dedicated to my parents, whose hard work laid the  
foundation for everything I have achieved....*

अपने माता-पिता को समर्पित, जिनकी कड़ी मेहनत ने मेरी हर उपलब्धि की  
नींव रखी....

# Certificate

This is to certify that the thesis entitled “**Turbulent Dispersion of Particles In the Wake of a Moving Vehicle**”, being submitted by **MANISH KUMAR** to the Indian Institute of Technology Delhi, for the award of the degree of **Doctor of Philosophy**, is a report of the bonafide research work carried out by him under our supervision. The thesis has been prepared in conformity with the rules and regulations of the Indian Institute of Technology, New Delhi, India. We further certify that the thesis has attained the standard required for a PhD degree of the Institute. The research reported, results presented in the thesis have not been submitted, in part or in full, to any other Institute or University for the award of any degree or diploma.



**Prof. Murali R. Cholevari**

Department of Applied Mechanics,  
Indian Institute of Technology Delhi.



**Prof. Srinivas V. Veeravalli**

Department of Applied Mechanics,  
Indian Institute of Technology Delhi.



**Prof. Mukesh Khare**

Civil Engineering Department,  
Indian Institute of Technology Delhi.

Date: February 2026

Place: New Delhi

# *Acknowledgements*

This PhD journey, with its inherent challenges, would not have been possible without the support, guidance, and encouragement of many individuals. To all of them, I extend my deepest and most sincere gratitude.

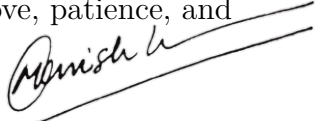
First and foremost, I would like to express my heartfelt gratitude to my parents, **Mr. Ramesh K. Mathur** and **Mrs. Kiran Mathur**, whose unwavering support and encouragement have been the foundation of my journey. Their belief in me has always been my greatest strength.

I extend my sincere thanks to everyone who has been a part of my research journey at IIT Delhi. I am deeply grateful to my PhD supervisors, Prof. Srinivas V. Veeravalli, Prof. Murali R. Cholehari, and Prof. Mukesh Khare, for their invaluable guidance, encouragement, and mentorship throughout my doctoral work. Their insights not only helped me navigate complex research challenges but also taught me important lessons in resilience and life.

I am thankful to my friends and colleagues at the Gas Dynamics Laboratory, Sri Hari, Adhitya and Anagh and at the CFD Lab., Dr. Sandeep Yadav, Dr. Tej Pratap, and Shivam, for their constant motivation, camaraderie, and support in overcoming both technical and non-technical hurdles. I would also like to acknowledge the skilled technical staff at the Department of Applied Mechanics. Their consistent willingness to help and support, particularly during the experimental phases of my work, was invaluable and greatly appreciated.

A very special and profound thank you goes to my wife, Dr. Bhumika, for being my constant source of strength. Her unwavering support, emotionally, physically, and even technically, during challenging times, has been invaluable. My deepest love also goes to my son, Vedant K. Mathur, his arrival has brought a new sense of purpose and immense joy to the final stages of this journey.

Finally, I am deeply grateful to all my family members for their love, patience, and encouragement throughout this journey.



**Manish Kumar**

# *Abstract*

Air pollution caused by particulate matter (PM) has emerged as a critical environmental issue, contributing significantly to ambient air particulates in urban areas and posing severe health risks to the population. Movement of the vehicle causes turbulent mixing of these pollutants due to the wake produced, and therefore increases the PM levels in the environment. The dispersion phenomenon in the wake is complex, governed by the three-dimensional vortical structures. Identifying and understanding the large-scale turbulent structures and wake topology is, therefore, fundamental to understand the pollutant dispersion phenomenon. However, detailed experimental investigations measuring and quantifying dispersion, especially under realistic moving ground conditions and linking dispersion directly to wake flow topologies, remain limited.

This thesis presents a comprehensive experimental investigation into the turbulent dispersion of smoke particles (a passive scalar) in the near wake of a simplified vehicle model (Ahmed body). The primary objective was to understand the complex correlation between turbulent flow structures and dispersion behaviour in the vehicle wake, focusing on the influence of vehicle rear slant angle ( $\phi = 15^\circ, 25^\circ, 35^\circ, \text{ and } 40^\circ$ ) and wind tunnel ground conditions. To achieve this, a dedicated experimental facility was developed, including a Rolling Road (RR) mechanism and an upstream Boundary Layer Suction (BLS) system. Testing and evaluation confirmed the effectiveness of the RR and BLS system by significantly reducing the oncoming boundary layer thickness (reduction in  $\delta \approx 70\%$ , and in  $\delta_1, \delta_2 \geq 95\%$ ), thereby minimizing the ground effects due to a stationary/fixed wind tunnel floor.

Advanced optical measurement techniques were employed for detailed flow and dispersion characterization. Particle Image Velocimetry (PIV) was used to obtain the velocity fields and identify dominant turbulent structures in the wake for different experimental configurations. A novel optical field measurement technique, Quantitative Smoke Visualization (QSV), similar to Planar Laser-Induced Fluorescence (PLIF) but adapted for laser Mie-scattering from smoke particles, was developed and implemented. This technique enabled spatially and temporally resolved measurements of instantaneous and time-averaged scalar (smoke particle) concentration fields.

The experimental results revealed critical dependencies of near-wake flow topology and particle dispersion on both the rear slant angle ( $\phi$ ) and the wind tunnel ground conditions (stationary/moving). PIV measurements confirmed that  $\phi$  significantly alters the wake topology, particularly the existence, size, and strength of key flow structures. For instance, strong trailing vortices dominate the wake at  $\phi = 25^\circ$ , while they are absent at  $\phi = 40^\circ$ , which features more dominant spanwise structures due to massive flow separation at the rear slant. Correspondingly, QSV measurements showed distinct dispersion patterns and concentration distributions directly linked to these flow topology changes; trailing vortices at  $\phi = 25^\circ$  significantly influenced dispersion patterns, whereas dispersion appeared more uniform behind the  $\phi = 40^\circ$  model.

Furthermore, comparing experiments with stationary and moving ground conditions revealed significant differences in flow topologies impacting dispersion. PIV results showed altered spanwise flow structures near the ground, in the stationary case, including the formation of an additional spanwise vortex (vortex G), not observed with the moving ground. To facilitate quantitative analysis of dispersion, novel dispersion parameters ( $\mathcal{D}$ ,  $\mathcal{L}_y$ ,  $\mathcal{L}_z$ ) were defined based on the concentration fields to characterize dispersion. Dispersion analysis confirmed that the altered structures directly enhance vertical mixing, leading to a higher overall non-dimensional dispersion ( $\Delta\mathcal{D} \approx 30 - 38\%$  increase) and vertical dispersion length scales ( $\Delta\mathcal{L}_y \approx 29 - 49\%$  increase) with the stationary ground compared to the moving ground case. Lateral dispersion ( $\mathcal{L}_z$ ), however, was found to be less influenced by the ground condition. These findings underscore the critical necessity of accurate ground simulation for wake dispersion studies in the wind tunnel. The findings are significant as they reveal that relying solely on stationary ground experiments leads to an overestimation of pollutant dispersion capacity and can create a false confidence (or sense of security) in pollution level estimates. The moving ground simulation, which is more representative of real-world conditions, showed significantly reduced dispersion, implying that actual near-wake pollution levels are much higher and persistent than predicted by stationary ground results.

## सारांश

कणिकीय पदार्थ (PM) के कारण होने वाला वायु प्रदूषण एक गंभीर पर्यावरणीय मुद्दा बन गया है, जो शहरी क्षेत्रों में परिवेशी वायु कणों में महत्वपूर्ण योगदान देता है और जनसंख्या के लिए गंभीर स्वास्थ्य जोखिम पैदा करता है। वाहन की गति से उत्पन्न वेक के कारण इन प्रदूषकों का अशांत मिश्रण होता है, और इसलिए पर्यावरण में PM के स्तर में वृद्धि होती है। वेक में फैलाव की घटना जटिल है, जो त्रि-आयामी भंवर संरचनाओं द्वारा नियंत्रित होती है। इसलिए, बड़े पैमाने पर अशांत संरचनाओं और वेक टोपोलॉजी (wake topology) को पहचानना और समझना प्रदूषक फैलाव की घटना को समझने के लिए मौलिक है। हालांकि, फैलाव को मापने और निर्धारित करने वाले विस्तृत प्रायोगिक अध्ययन, विशेष रूप से यथार्थवादी गतिशील जमीनी परिस्थितियों में और फैलाव को सीधे वेक प्रवाह टोपोलॉजी से जोड़ने वाले अध्ययन सीमित हैं।

यह शोध प्रबंध एक सरलीकृत वाहन मॉडल (Ahmed body) के निकट वेक में धुएं के कणों (एक निष्क्रिय अदिश) के अशांत फैलाव में एक व्यापक प्रायोगिक जांच प्रस्तुत करती है। प्राथमिक उद्देश्य पवन सुरंग की स्थितियों में वाहन वेक में अशांत प्रवाह संरचनाओं और फैलाव व्यवहार के बीच जटिल संबंध को समझना था, जिसमें वाहन के पिछले हिस्से की ज्यामिति (पिछला ढलान कोण,  $\phi = 15^\circ, 25^\circ, 35^\circ$ , और  $40^\circ$ ) और पवन सुरंग की जमीनी स्थितियों के प्रभाव पर ध्यान केंद्रित किया गया था। इस लक्ष्य को प्राप्त करने के लिए, एक समर्पित प्रायोगिक सुविधा विकसित की गई, जिसमें एक Rolling Road (RR) तंत्र और एक अपस्ट्रीम Boundary Layer Suction (BLS) प्रणाली शामिल थी। परीक्षण और मूल्यांकन ने यथार्थवादी गतिशील जमीनी स्थितियों का अनुकरण करने में RR और BLS प्रणाली की प्रभावशीलता की पुष्टि की, जिससे आने वाली बाउंड्री लेयर (boundary layer) की मोटाई में उल्लेखनीय कमी आई (लगभग 70% की कमी, और  $\delta_1, \delta_2 \geq 95\%$  में कमी), जिससे एक स्थिर/निश्चित पवन सुरंग के फर्श के कारण होने वाले जमीनी प्रभावों को कम किया जा सके।

विस्तृत प्रवाह और फैलाव लक्षण वर्णन के लिए उन्नत ऑप्टिकल माप तकनीकों का उपयोग किया गया। विभिन्न प्रायोगिक विन्यासों के लिए वेक में वेग क्षेत्रों को प्राप्त करने और प्रमुख अशांत संरचनाओं की पहचान करने के लिए Particle Image Velocimetry (PIV) का उपयोग किया गया। एक नई ऑप्टिकल क्षेत्र माप तकनीक, Quantitative Smoke Visualization (QSV), जो Planar Laser-Induced Fluorescence (PLIF) के समान है, लेकिन धुएं के कणों से लेजर मी-स्कैटरिंग के लिए अनुकूलित है, विकसित और

कार्यान्वित की गई। इस तकनीक ने तात्कालिक और समय-औसत अदिश (धुएं के कण) सांद्रता क्षेत्रों के स्थानिक और अस्थायी रूप से हल किए गए मापों को सक्षम किया।

प्रायोगिक परिणामों ने पिछले ढलान कोण ( $\phi$ ) और पवन सुरंग की जमीनी स्थितियों (स्थिर/गतिशील) दोनों पर निकट-वेक प्रवाह टोपोलॉजी और कण फैलाव की महत्वपूर्ण निर्भरता का खुलासा किया। PIV मापों ने पुष्टि की कि  $\phi$  वेक टोपोलॉजी को महत्वपूर्ण रूप से बदलता है, विशेष रूप से प्रमुख प्रवाह संरचनाओं का अस्तित्व, आकार और शक्ति। उदाहरण के लिए,  $\phi = 25^\circ$  पर मजबूत trailing भंवर वेक पर हावी होते हैं, जबकि  $\phi = 40^\circ$  पर वे अनुपस्थित होते हैं, जिसमें पिछले ढलान पर बड़े पैमाने पर प्रवाह अलगाव के कारण अधिक प्रमुख spanwise संरचनाएं होती हैं। तदनुसार, QSV मापों ने इन प्रवाह टोपोलॉजी परिवर्तनों से सीधे जुड़े हुए अलग-अलग फैलाव पैटर्न और सांद्रता वितरण दिखाए;  $\phi = 25^\circ$  पर trailing भंवरों ने फैलाव पैटर्न को महत्वपूर्ण रूप से प्रभावित किया, जबकि  $\phi = 40^\circ$  मॉडल के पीछे फैलाव अधिक समान दिखाई दिया।

इसके अलावा, स्थिर और गतिशील जमीनी स्थितियों के साथ प्रयोगों की तुलना से फैलाव को प्रभावित करने वाली प्रवाह टोपोलॉजी में महत्वपूर्ण अंतर का पता चला। PIV परिणामों ने स्थिर मामले में जमीन के पास बदली हुई spanwise प्रवाह संरचनाएं दिखाई, जिसमें एक अतिरिक्त spanwise भंवर (vortex G) का निर्माण भी शामिल है, जो गतिशील जमीन के साथ नहीं देखा गया था। फैलाव के मात्रात्मक विश्लेषण को सुविधाजनक बनाने के लिए, फैलाव को चिह्नित करने के लिए सांद्रता क्षेत्रों के आधार पर नए फैलाव पैरामीटर ( $\mathcal{D}$ ,  $\mathcal{L}_y$ ,  $\mathcal{L}_z$ ) परिभाषित किए गए थे। फैलाव विश्लेषण ने पुष्टि की कि इन बदली हुई संरचनाओं ने सीधे ऊर्ध्वाधर मिश्रण को बढ़ाया, जिससे स्थिर जमीन के साथ गतिशील जमीन के मामले की तुलना में उच्च समग्र गैर-आयामी फैलाव ( $\Delta \mathcal{D} \approx 30 - 38\%$  की वृद्धि) और काफी बड़े ऊर्ध्वाधर फैलाव लंबाई पैमाने ( $\Delta \mathcal{L}_y \approx 29 - 49\%$  की वृद्धि) हुए। हालांकि, पार्श्व फैलाव ( $\mathcal{L}_z$ ) जमीनी स्थिति से कम प्रभावित पाया गया। ये निष्कर्ष पवन सुरंग में वेक फैलाव अध्ययनों के लिए सटीक जमीनी अनुकरण की महत्वपूर्ण आवश्यकता को रेखांकित करते हैं।

ये निष्कर्ष महत्वपूर्ण हैं क्योंकि ये दर्शाते हैं कि केवल स्थिर जमीनी प्रयोगों पर निर्भर रहने से प्रदूषक फैलाव क्षमता का अति-आकलन हो जाता है और प्रदूषण स्तर के अनुमानों में एक गलत विश्वास (या सुरक्षा की भावना) पैदा हो सकती है। गतिशील जमीनी सिमुलेशन, जो वास्तविक दुनिया की स्थितियों का अधिक प्रतिनिधि है, ने फैलाव में उल्लेखनीय कमी दिखाई, जिसका अर्थ है कि वास्तविक निकट-जागृति प्रदूषण स्तर स्थिर जमीनी परिणामों द्वारा अनुमानित स्तर से कहीं अधिक और स्थायी है।

# Contents

Certificate

Acknowledgements

Abstract

Contents

List of Figures

List of Tables

Abbreviations

Symbols

<b>1</b>	<b>Introduction</b>	<b>1</b>
1.1	State of Global Air . . . . .	1
1.2	Impact of Air Pollution on Human Health . . . . .	2
1.3	Air Pollutants from Vehicular Movements . . . . .	4
1.4	Motivation . . . . .	6
1.5	Thesis Organisation . . . . .	7
<b>2</b>	<b>Literature Review</b>	<b>9</b>
2.1	Vehicle Wake Definition and Flow Structures . . . . .	10
2.2	Simplified Vehicle Models for Wake Studies . . . . .	14
2.3	Flow Topology of Ahmed Body Wake . . . . .	16
2.4	Dispersion in the Wake of Vehicle Model . . . . .	22
2.5	Wind Tunnel Ground Effects on Dispersion in the Vehicle Wake . . . . .	26
2.6	Research Gaps in the Literature . . . . .	31

2.7	Objectives of the Study . . . . .	34
<b>3</b>	<b>Development of Experimental Setup and the Measurement Techniques</b>	<b>37</b>
3.1	Modification of Environmental Wind Tunnel . . . . .	38
3.2	Design of Rolling Road Mechanism . . . . .	39
3.3	Design of Boundary Layer Suction System . . . . .	40
3.4	Testing of Rolling Road and Boundary Layer Suction System . . . . .	42
3.5	Concentration Field Measurement Technique: Quantitative Smoke Visualization . . . . .	48
3.5.1	The Beer-Lambert law in Planar Laser Induced Fluorescence (PLIF) and its connection to Mie scattering . . . . .	48
3.5.1.1	Correction for the laser attenuation . . . . .	52
3.5.1.2	Geometric correction . . . . .	55
3.5.2	Calibration for concentration measurements . . . . .	56
3.5.2.1	Calibration results . . . . .	60
3.5.3	Extinction coefficient $\zeta$ . . . . .	63
3.5.4	Experiments for determining passive nature and buoyancy effects of the smoke . . . . .	67
3.6	Experimental Setup for QSV Measurements . . . . .	71
3.7	Experimental Measurements and Discussion . . . . .	75
3.7.1	Concentration field measurements in the Ahmed body wake . . . . .	76
3.7.2	Error analysis . . . . .	79
3.7.2.1	Errors in a typical instantaneous field . . . . .	80
3.7.2.2	Estimation of the RMS error . . . . .	81
3.8	Setup for Particle Image Velocimetry (PIV) . . . . .	83
3.8.1	PIV measurements in model mid-plane . . . . .	83
3.8.2	PIV measurements in cross-stream plane . . . . .	85
3.9	Chapter Summary . . . . .	86
<b>4</b>	<b>Experiments on Fixed Ground: Effects of Rear Slant Angle on Flow Topology and Dispersion in the Near Wake</b>	<b>89</b>
4.1	Smoke Visualisations: Smoke Dispersion at the Rear End . . . . .	91
4.2	PIV Results: Dominating Flow Structures . . . . .	95
4.2.1	Longitudinal structures . . . . .	95
4.2.2	Spanwise structures . . . . .	97
4.3	Concentration Field Measurements . . . . .	103
4.3.1	Effects of longitudinal trailing vortices on concentration distribution . . . . .	109
4.4	Estimates of Dispersion in the Ahmed Body Near Wake . . . . .	113
4.4.1	Non-dimensional dispersion ( $\mathcal{D}$ ) . . . . .	113
4.4.2	Dispersion length scales ( $\mathcal{L}_y, \mathcal{L}_z$ ) . . . . .	120

4.5	Time-averaged Flow Structures and Dispersion Phenomenon in the Near Wake . . . . .	123
4.6	Characteristics of Ahmed Body Near Wake Based on Dispersion . . .	126
4.7	Chapter Summary and Conclusions . . . . .	129
<b>5</b>	<b>Experiments on Moving Ground: Effect of Wind Tunnel Ground Conditions on Flow Topology and Dispersion in the Near Wake</b>	<b>133</b>
5.1	Test Conditions and Vehicle Model . . . . .	134
5.2	PIV Results: Spanwise Flow Structures in the Near Wake . . . . .	136
5.2.1	Critical flow points . . . . .	140
5.2.2	Recirculation region . . . . .	141
5.3	Concentration Field Measurements . . . . .	144
5.4	Estimates of Dispersion in the Ahmed Body Near Wake . . . . .	148
5.4.1	Non-dimensional dispersion ( $\mathcal{D}$ ) . . . . .	148
5.4.2	Dispersion length scales ( $\mathcal{L}_y, \mathcal{L}_z$ ) . . . . .	151
5.5	Chapter Summary and Conclusions . . . . .	156
<b>6</b>	<b>Conclusions and Future work</b>	<b>159</b>
6.1	Conclusions . . . . .	159
6.2	Implications and Contributions of the Present Study . . . . .	162
6.3	Scope for Future Work . . . . .	165
<b>A</b>	<b>Design and Details of the Experimental Setup</b>	<b>169</b>
A.1	Contraction and Flexible Coupling for Environmental Wind Tunnel .	169
A.2	Design of the Major Components of Rolling Road . . . . .	170
A.3	Design Parameters for Boundary Layer Suction . . . . .	172
A.4	Boundary Layer Parameters from Velocity Measurements . . . . .	173
A.5	QSV Calibration for 1200W Smoke Machine . . . . .	175
	<b>Bibliography</b>	<b>177</b>
	<b>Author Biodata and List of Publications from the Present Work</b>	<b>189</b>

# List of Figures

1.1	The ten countries with the highest $PM_{2.5}$ exposures worldwide. Data from Special Report on State of Global Air 2020 by Health Effects Institute (2020) . . . . .	2
1.2	Global ranking of risk factors by total number of deaths from all causes in 2021. Data from Special Report on State of Global Air 2024 by Health Effects Institute (2024). . . . .	3
1.3	Death rate per 100,000 attributable to air pollution ( $PM_{2.5}$ ) in 2023 worldwide. The data in the map has been taken from the ‘Special Report on State of Global Air 2025’ by Health Effects Institute (2025). . . . .	3
1.4	(a) Vehicular exhaust emissions dispersion in the wake of a car (source: internet). (b) Non-exhaust emissions dispersion in the wake of a public transport bus (Photo by the Author, Adhchini Gate, IIT Delhi, India). . . . .	5
2.1	Visualisation of the wake behind a typical moving vehicle using smoke (adapted from Ahmed (1983)). . . . .	10
2.2	Definition of near and far wake regions behind a typical moving vehicle (Baker, 2001, Hucho, 2013). . . . .	11
2.3	Spanwise vortices in the recirculation region (shown by the streamlines) behind a vehicle model with different rear slant angle ( $\phi$ ) (Adapted from Ahmed (1983)). . . . .	12
2.4	Schematic showing the formation of the trailing vortices on the C-pillar of the vehicle (adapted from Hucho et al. (1975)). . . . .	13
2.5	Dispersion of the particulates in the (a) near wake ( $x \leq 15H$ ) (Photo by the Author, Khardungla pass, Leh-Ladakh), and (b) far wake ( $x \geq 15H$ ) (source: internet). . . . .	13
2.6	Schematic diagram of the Ahmed body model (as first used by Ahmed et al. (1984)) with dimensions. Rear slant angle ( $\phi$ ) and the coordinate system $O(x, y, z)$ used in the present study are also shown. . . . .	15
2.7	Typical Indian passenger cars shapes (a) Maruti Suzuki-Breeza, SUV (2023), (b) Maruti Suzuki-Fronx, SUV (2024) . . . . .	16
2.8	A schematic diagram of the flow pattern behind the Ahmed body model is shown (adapted from Ahmed et al. (1984)). . . . .	17

2.9	A conceptual model of the flow structure around the Ahmed body in the (a) high drag regime ( $\phi = 25^\circ$ ) and (b) low drag regime ( $\phi = 35^\circ$ ). Adapted from Zhang et al. (2015) and Liu et al. (2021) respectively. .	20
2.10	Mean temperature excess behind $\phi = 25^\circ$ Ahmed body at (a) $x/h = 0.25$ (b) $x/h = 1$ and (c) $x/h = 5$ . Adapted from Gosse et al. (2006a)	24
2.11	Schematic showing the (a) actual road conditions and (b) wind tunnel simulation (obtained essentially by applying a Galilean transformation).	27
2.12	Vertical profiles of dimensionless concentration ( $C^*$ ) from the wind tunnel tests in the ‘EnFlo’ (1:5 model) and ‘Aero’ (1:8 model, with and without rolling road operation) tunnels (Carpentieri et al., 2012).	30
3.1	Schematic diagram of the environmental wind tunnel with the rolling road. (a) Top view of the wind tunnel. (b) A 3D model of the rolling system with the boundary layer suction. . . . .	39
3.2	The (a) side view and (b) top view of asymmetric contraction for the wind tunnel to accommodate the rolling road. . . . .	40
3.3	Schematic showing the rolling road technique along with the boundary layer suction system. . . . .	41
3.4	Boundary layer suction system and its components. . . . .	42
3.5	Experimental setup for boundary layer measurements in the wind tunnel test section. . . . .	43
3.6	Schematic of the velocity measurement locations (a) in the streamwise direction and (b) in the cross-stream direction. . . . .	43
3.7	Comparison of the non-dimensional velocity $u(y)/U_\infty$ in the boundary layer, for the stationary and moving ground case at different streamwise locations; $x = 10\text{ cm}$ , $20\text{ cm}$ , $30\text{ cm}$ , $50\text{ cm}$ , $70\text{ cm}$ and $100\text{ cm}$ in the wind tunnel test section. . . . .	45
3.8	Non-dimensional velocity $u(y)/U_\infty$ profiles on the moving ground (with boundary layer suction) system at five cross-stream locations; $z = \pm 28\text{ cm}$ , $\pm 14\text{ cm}$ and $z = 0\text{ cm}$ at $x = 30\text{ cm}$ in the wind tunnel test section. . . . .	46
3.9	Variation of boundary layer thickness in streamwise direction on the wind tunnel floor for stationary ( $\delta_{st}$ ) and moving ( $\delta_{mv}$ ) ground case. .	47
3.10	Laser Mie-scattering by smoke particles. . . . .	50
3.11	The Beer-Lambert law and the attenuation of the laser when passing through smoke particles. The laser beam direction is from left to right. . . . .	52
3.12	Geometry of the non-parallel laser sheet in the measurement domain.	55
3.13	Schematic view of the experimental setup for the calibration. The field of view of the camera is also shown on the left, where $S(r)$ is obtained from the time-averaged calibration image, and $U(r)$ is obtained from the PIV measurements in the longitudinal plane. . . .	57

3.14	Calibration curve showing smoke concentration ( $\bar{C}$ ) in ppmw vs. signal intensity ( $\bar{S}$ ). The red region shows the regime of linear response of the signal (Linear regime). The blue region shows the regime of signal saturation (Saturation regime). The green region shows the range in which dispersion experiments are performed (typically, $\approx 12500 - 15000$ ppmw). The dashed red and blue lines are the linear fit to the experimental data in the linear and saturation regimes, respectively. . . . .	61
3.15	Signal intensity attenuation (before and after attenuation correction) along the laser-beam propagation path $x$ for smoke concentrations $\bar{C} = 14994$ ppmw. The black dashed lines are the linear fit to the experimentally measured data. The laser direction is from right to left.	63
3.16	(a) The schematic of the mixing duct is shown. The uncorrected and attenuation-corrected signal $S(x)$ from the region indicated by the yellow band is shown for smoke concentrations $\bar{C} = 14994$ ppmw. (b) Signal intensity attenuation (before and after attenuation correction) along the laser-beam propagation path for smoke concentrations $\bar{C} = 14994$ ppmw are shown (logarithm of the normalised obtained signal ( $\ln(S(x)/S_o)$ ) is plotted). . . . .	65
3.17	Schematic view of the experimental setup for the study of buoyancy effects of the smoke. . . . .	69
3.18	(a) Average plume paths for different free stream velocities $U_\infty$ , $x$ is streamwise distance and $y$ is cross-stream vertical distance, $(0,0)$ is the location of the smoke source. The (b) instantaneous and (c) time-averaged image of the plume (at $U_\infty = 0.9 \text{ ms}^{-1}$ ) are also shown. A horizontal plume path indicates the absence of any buoyancy effects.	70
3.19	Configuration of the detachable rear end of the Ahmed body with different rear slant angles ( $\phi = 15^\circ, 25^\circ, 35^\circ$ and $40^\circ$ ). All dimensions are in $mm$ . . . . .	72
3.20	Schematic view of the experimental set-up in the wind tunnel (diagram not to scale). . . . .	73
3.21	The schematic of the Quantitative Smoke Visualization (QSV) technique for concentration field measurements in the Ahmed body wake.	74
3.22	(a) Instantaneous image of smoke particles in the near wake of the Ahmed body ( $\phi = 25^\circ$ ) at $x^* = 0.25$ in the wind tunnel. Image taken from a downstream position behind Ahmed body in the wind tunnel. Yellow arrows show the formation and direction of trailing vortices. The red dashed line shows the model midplane. (b) The time-averaged image (average of approximately 2000 instantaneous frames) in the near wake of the Ahmed body ( $\phi = 25^\circ$ ) at $x^* = 0.25$ in the wind tunnel. . . . .	76

3.23	Concentration contours at $x^* = 0.25$ behind Ahmed body ( $\phi = 25^\circ$ ) are shown. The results are compared with the point measurements of Gosse et al. (2006a). (a) Mean temperature excess ( $\langle T^* \rangle$ ) (Gosse et al., 2006a). (b) Non-dimensionalised mean concentration ( $\langle C^* \rangle$ ) (Current study) – No attenuation correction. (c) Non-dimensionalised mean concentration ( $\langle C^* \rangle$ ) (Current study) – Only geometric correction. (d) Non-dimensionalised mean concentration ( $\langle C^* \rangle$ ) (Current study) – Full attenuation correction. The effect of attenuation correction on the accuracy of the mean concentration fields is shown. . . . .	78
3.24	Comparison of the instantaneous concentration field obtained at $x^* = 0.25$ behind Ahmed body after (a) no correction, (b) geometric correction, and (c) full attenuation correction. The laser beam is from right to left. . . . .	80
3.25	Schematic of the PIV setup for velocity measurements in the Ahmed body midplane, top view of the wind tunnel section is shown. . . . .	84
3.26	Schematic of the PIV setup for velocity measurements in the Ahmed body midplane. The laser sheet used for illumination and the coordinate system are shown. . . . .	84
3.27	Schematic of the PIV setup for measurements in the cross-stream plane, top view of the wind tunnel test section is shown. . . . .	85
4.1	Planes of measurements in the near wake of the Ahmed body. Planes A, B and C are rear vertical planes behind Ahmed body at $x^* = 0.25, 1$ and $5$ respectively, and Plane D is $x - y$ plane in line with the source location. . . . .	90
4.2	Instantaneous images showing the typical flow of smoke in the plane of source (i.e. $x-y$ plane at $z^* = -0.31$ ) at $Re_l = 1.90 \times 10^5$ behind the Ahmed body (a) $\phi = 15^\circ$ , (b) $\phi = 25^\circ$ , (c), $\phi = 35^\circ$ , and (d) $\phi = 40^\circ$ . The envelope of the smoke is also shown by the solid yellow line. The flow is from right to left. . . . .	92
4.3	Instantaneous images showing the typical flow of smoke in the rear vertical plane (i.e. $y-z$ plane) at $x^* = 0.25$ at $Re_l = 1.90 \times 10^5$ behind the Ahmed body (a) $\phi = 15^\circ$ , and (b) $\phi = 25^\circ$ , (c) $\phi = 35^\circ$ , and (d) $\phi = 40^\circ$ . The flow direction is out of the paper. . . . .	93
4.4	(a) Time-averaged velocity vectors in the $y - z$ plane at $x^* = 0.25$ obtained from PIV measurements, behind Ahmed body $\phi = 25^\circ$ model. (b) Time-averaged streamwise vorticity $\langle \omega_x \rangle$ in the cross-stream ( $y - z$ ) plane at $x^* = 0.25$ obtained from PIV measurements behind the Ahmed body ( $\phi = 25^\circ$ ). The flow direction is out of the paper. Contour cut off levels are $\langle \omega_x \rangle = \pm 0.1 \text{ sec}^{-1}$ . The outline of Ahmed body and the smoke source are also shown. . . . .	96
4.5	Time-averaged velocity field in the recirculation region obtained from PIV measurements in model mid plane ( $x - y$ ) at $z^* = 0$ , behind the	98

4.6	Time-averaged streamlines obtained from PIV measurements in the recirculation region behind the Ahmed body model (a) $\phi = 25^\circ$ and (b) $\phi = 40^\circ$ in midplane $x - y$ . The upper and lower vortices formed in the recirculation region are shown. Flow direction is from right to left. . . . .	99
4.7	Time-averaged vorticity iso-contours $\langle \omega_z \rangle$ in the midplane $z^* = 0$ , behind Ahmed body model (a) $\phi = 25^\circ$ and (b) $\phi = 40^\circ$ . Contours cut off levels are $\langle \omega_z \rangle = \pm 0.25 \text{ sec}^{-1}$ . . . . .	101
4.8	Non-dimensional mean concentration $\langle C^*(y, z) \rangle$ contours in the near wake of the Ahmed body with different rear slant angles (a) $\phi = 15^\circ$ , (b) $\phi = 25^\circ$ , (c) $\phi = 35^\circ$ , and (d) $\phi = 40^\circ$ at downstream location $x^* = 0.25$ . . . . .	104
4.9	Non-dimensional mean concentration $\langle C^*(y, z) \rangle$ contours in the near wake of the Ahmed body with different rear slant angles (a) $\phi = 15^\circ$ , (b) $\phi = 25^\circ$ , (c) $\phi = 35^\circ$ , and (d) $\phi = 40^\circ$ at downstream location $x^* = 1$ . . . . .	105
4.10	Non-dimensional mean concentration $\langle C^*(y, z) \rangle$ contours in the near wake of the Ahmed body with different rear slant angles (a) $\phi = 15^\circ$ , (b) $\phi = 25^\circ$ , (c) $\phi = 35^\circ$ , and (d) $\phi = 40^\circ$ at downstream location $x^* = 5$ . . . . .	107
4.11	Non-dimensional mean concentration $\langle C^* \rangle$ vs. $z^*$ , plotted at $x^* = 0.25$ , $y^* = 0.92$ , (Present study) and non-dimensional mean temperature excess $\langle T^* \rangle$ vs $z^*$ , plotted at $x^* = 0$ , $y^* = 0.92$ (Gosse et al. (2006c)) . . . . .	110
4.12	Non-dimensional mean concentration $\langle C^* \rangle$ vs $z^*$ plotted at the height of Ahmed body rear slant trailing edge (refer to Table 4.1) at (a) $x^* = 0.25$ (b) $x^* = 1$ , and at $y^* = 0.5$ at (c) $x^* = 5$ in the near wake. . . . .	111
4.13	Schematic showing the procedure of obtaining the dispersion parameters ( $\mathcal{D}$ , $\mathcal{L}_y$ , and $\mathcal{L}_z$ ) from the concentration field measurements. The Dispersion envelope is shown by a solid blue line behind the Ahmed body ( $\phi = 25^\circ$ ) at the downstream location $x^* = 0.25$ . The red box shows the equivalent dispersion rectangle. The height ( $h_r$ ) and width ( $b_r$ ) of the rectangle are shown. . . . .	115
4.14	Dispersion envelope is shown by solid blue line behind Ahmed body ( $\phi = 40^\circ$ ) at downstream location (a) $x^* = 0.25$ , (b) $x^* = 1$ , and (c) $x^* = 5$ . The red box shows the equivalent dispersion rectangle obtained by equating $I_{zz}$ , $I_{yy}$ and the centroid of the dispersion envelope. The height ( $h_r$ ) and width ( $b_r$ ) of the rectangle are shown. . . . .	116
4.15	(a) Non-dimensional dispersion $\mathcal{D}$ vs. streamwise distance $x^*$ , for different rear slant angles of Ahmed body. (b) The relative change in the non-dimensional dispersion $\Delta \mathcal{D}_{rel} / \Delta x^*$ vs. streamwise distance $x^*$ in the Ahmed body wake for different rear slant angles. . . . .	117

4.16	Variation of dispersion length scales in vertical ( $\mathcal{L}_y$ ) and lateral ( $\mathcal{L}_z$ ) directions w.r.t. Ahmed body rear slant angle ( $\phi$ ) at three downstream locations (a) $x^* = 0.25$ (b) $x^* = 1$ (c) $x^* = 5$ . . . . .	122
4.17	Schematic of time-averaged three-dimensional flow structures in the wake of the Ahmed body for different rear slant angles (a) $\phi = 15^\circ$ , (b) $\phi = 25^\circ$ , (c) $\phi = 35^\circ$ , and (d) $\phi = 40^\circ$ . The formation of trailing vortices at rear slant edges (C-pillars) and the direction are shown, and the downwash created by the trailing vortices is shown by red arrows. For angles $\phi = 15^\circ, 25^\circ$ , flow separation takes place at the trailing edge of the rear slant (as shown); for $\phi = 35^\circ, 40^\circ$ flow separation takes place at the leading edge (shown by the blue line) of the rear slant, backflow over the rear slant is shown by arrows. The flow is from left to right. . . . .	124
4.18	Characteristics of Ahmed body near-wake, based on the particulate dispersion. The two regions of the near wake ( <i>early near-wake</i> and <i>late near-wake</i> ) are shown for both the flow regimes; (a) subcritical ( $\phi < \phi_c$ ) and (b) supercritical ( $\phi > \phi_c$ ) rear slant angle. . . . .	127
5.1	Dimensions of the modified Ahmed body with wheel and smoke source.	134
5.2	Schematic of the experimental setup for scalar concentration measurements. The moving ground and boundary layer suction slot is shown, along with a modified Ahmed body with a smoke machine kept inside. . . . .	135
5.3	Time-averaged velocity field in the wake, obtained from PIV measurements in the model midplane at $z^* = 0$ , behind the Ahmed body with rear slant angles of (a-b) $\phi = 25^\circ$ and (c-d) $40^\circ$ for both stationary and moving ground conditions. Flow is from left to right. . . . .	137
5.4	Time averaged streamlines in the near wake, obtained from PIV measurements in the model midplane at $z^* = 0$ behind the Ahmed body with rear slant angles of (a-b) $\phi = 25^\circ$ and (c-d) $\phi = 40^\circ$ for both stationary and moving ground conditions. The critical flow points in the wake are also shown. Flow is from left to right. . . . .	139
5.5	Locations of critical flow points ( $F_1, F_2$ and SP) in the near wake of the Ahmed body with rear slant angles (a) $\phi = 25^\circ$ and (b) $\phi = 40^\circ$ for stationary and moving ground conditions. . . . .	141
5.6	Iso-contours of time-averaged spanwise vorticity $\langle \omega_z \rangle$ in the model midplane plane $z^* = 0$ behind the Ahmed body with slant angles of (a-b) $\phi = 25^\circ$ and (c-d) $\phi = 40^\circ$ for both stationary and moving ground conditions. Contours cut-off levels are $\langle \omega_z \rangle = \pm 0.25 \text{ sec}^{-1}$ . . .	143
5.7	Concentration $\langle C^*(y, z) \rangle$ contours in the near wake of Ahmed body with $\phi = 25^\circ$ (in $y - z$ plane at different $x^*$ locations) for stationary and moving ground conditions. . . . .	145

5.8	Concentration $\langle C^*(y, z) \rangle$ contours in the near wake of Ahmed body with $\phi = 40^\circ$ (in $y - z$ plane at different $x^*$ locations) for stationary and moving ground conditions. . . . .	146
5.9	Variation of non-dimensional dispersion ( $\mathcal{D}$ ) w.r.t. downstream distance in the wake of Ahmed body with slant angle $\phi = 25^\circ$ and $40^\circ$ . .	149
5.10	Variation of non-dimensional dispersion length scales in vertical ( $\mathcal{L}_y$ ) directions w.r.t. downstream distance ( $x^*$ ) in the wake of Ahmed body with rear slant angles $\phi = 25^\circ$ and $40^\circ$ . . . . .	152
5.11	Variation of non-dimensional dispersion length scales in lateral ( $\mathcal{L}_z$ ) directions w.r.t. downstream distance ( $x^*$ ) in the wake of Ahmed body with rear slant angles $\phi = 25^\circ$ and $40^\circ$ . . . . .	153
5.12	Schematic representation of the flow structures for stationary and moving ground conditions in the near wake of the Ahmed body with rear slant angles $\phi = 25^\circ$ and $\phi = 40^\circ$ . . . . .	155
A.1	Side and Isometric view of the flexible coupling between suction fan and wind tunnel test section. . . . .	170
A.2	Structural analysis of the platen. The contours of platen deformation are shown (units of deformation are in $m$ ). . . . .	171
A.3	Variation of displacement thickness in stream-wise direction on the wind tunnel floor for stationary ( $\delta_{st}$ ) and moving ( $\delta_{mv}$ ) ground case. .	174
A.4	Variation of momentum thickness in stream-wise direction on the wind tunnel floor for stationary ( $\delta_{2st}$ ) and moving ( $\delta_{2mv}$ ) ground case. .	175
A.5	Calibration curve for 1200 W smoke machine. The green region shows the concentration range in which all the dispersion experiments (on rolling road) were performed. . . . .	176

# List of Tables

2.1	Summary of studies (Experimental and CFD) on the wake flow characteristics of the Ahmed body. . . . .	23
2.2	Summary of studies (Experimental and CFD) on the scalar dispersion in the turbulent wake of the Ahmed body. . . . .	27
2.3	Comparison of Existing Literature on Ahmed Body Wake Studies with the Present Work. . . . .	32
3.1	Boundary layer thickness $\delta$ (for stationary ( $\delta_{st}$ ) and moving ( $\delta_{mv}$ ) ground case) and reduction in boundary layer thickness $Reduction_{\delta}$ (in percentage) at different downstream locations on the rolling road. . . . .	47
3.2	Signal intensity attenuation (in percentage) along the laser path before attenuation correction for various absolute smoke concentrations released in the mixing duct during calibration. . . . .	66
3.3	Signal intensity attenuation (in percentage) along the laser path after the attenuation correction by an iterative method (Cholemari et al., 2024, Cholemari and Vishnubhatla, 2024) for various absolute smoke concentrations released in the mixing duct during calibration. . . . .	67
3.4	Location of the smoke source given in non-dimensionalised coordinates, for the present study and Gosse et al. (2006a). . . . .	79
3.5	The RMSN errors resulting when the attenuation correction is either not done (Uncorrected) or only when the intensity of the laser beam is adjusted for the spreading (Geometric correction). . . . .	82
4.1	Height of the rear slant trailing edge for different Ahmed body models given in terms of non-dimensional vertical distance ( $y^*$ ). . . . .	111
4.2	Lateral spread of the smoke at $y^* = 0.5$ , $x^* = 5$ for different rear slant angles of Ahmed body. . . . .	113
4.3	Non-dimensionalised dispersion ( $\mathcal{D} = A_c/A_m$ ) at downstream locations $x^* = 0.25$ , $x^* = 1$ and $x^* = 5$ in the Ahmed body wake. . . . .	116
4.4	Non-dimensional vertical ( $\mathcal{L}_y$ ) and lateral ( $\mathcal{L}_z$ ) dispersion length scales at downstream locations $x^* = 0.25$ , 1, and 5 in the Ahmed body wake for different rear slant angles $\phi$ . . . . .	121

5.1	Positions $(x^*, y^*)$ of critical flow points ( $F_1$ and $F_2$ ; upper and lower spanwise vortex core) in the recirculation region in the model mid-plane ( $z^* = 0$ ) . . . . .	140
5.2	Comparison of recirculation length ( $L_R^*$ ) for both ground conditions. . . . .	142
5.3	Non-dimensional dispersion ( $\mathcal{D} = A_c/A_m$ ) ( $A_c$ is the area of dispersion envelope, and $A_m = h \times b$ is the Ahmed body frontal area) at various downstream locations ( $x^*$ ) in the Ahmed body wake. . . . .	149
5.4	Non-dimensional vertical ( $\mathcal{L}_y$ ) at various downstream locations ( $x^*$ ) in the Ahmed body wake. . . . .	151
5.5	Non-dimensional lateral ( $\mathcal{L}_z$ ) at various downstream locations ( $x^*$ ) in the Ahmed body wake. . . . .	151
5.6	Increase in the non-dimensional dispersion parameters in the near wake of Ahmed body ( $\phi = 25^\circ$ ). . . . .	154
5.7	Increase in the non-dimensional dispersion parameters in the near wake of Ahmed body ( $\phi = 40^\circ$ ). . . . .	155
A.1	Constants of equation for wind tunnel contraction profile . . . . .	169
A.2	Boundary layer displacement thickness (for stationary ( $\delta_{1st}$ ) and moving ( $\delta_{1mv}$ ) ground case) and <i>Reduction</i> $_{\delta_1}$ (in percentage) at different downstream locations on the rolling road midplane. . . . .	174
A.3	Boundary layer momentum thickness $\delta_2$ (for stationary ( $\delta_{2st}$ ) and moving ( $\delta_{2mv}$ ) ground case) and reduction in the momentum thickness <i>Reduction</i> $_{\delta_2}$ (in percentage) at different downstream locations on the rolling road. . . . .	175

# Abbreviations

<b>ADHD</b>	<b>A</b> ttention <b>D</b> eficit <b>H</b> yperactivity <b>D</b> isorder
<b>ADMS</b>	<b>A</b> tmospheric <b>D</b> ispersion <b>M</b> odelling <b>S</b> oftware
<b>CFL</b>	<b>C</b> ourant <b>F</b> riedrichs <b>L</b> ewy
<b>CFD</b>	<b>C</b> omputational <b>F</b> luid <b>D</b> ynamics
<b>CWT</b>	<b>C</b> old <b>W</b> ire <b>T</b> hermometry
<b>ELPI</b>	<b>E</b> lectrical <b>L</b> ow <b>P</b> ressure <b>I</b> mpactor
<b>IDDES</b>	<b>I</b> mproved <b>D</b> elayed <b>D</b> etached <b>E</b> ddy <b>S</b> imulation
<b>FFID</b>	<b>F</b> ast <b>F</b> lame <b>I</b> onisation <b>D</b> etector
<b>FID</b>	<b>F</b> lame <b>I</b> onisation <b>D</b> etector
<b>FOV</b>	<b>F</b> ield <b>O</b> f <b>V</b> iew
<b>LDA</b>	<b>L</b> aser <b>D</b> opler <b>A</b> nemometry
<b>LDV</b>	<b>L</b> aser <b>D</b> opler <b>V</b> elocimetry
<b>LPT</b>	<b>L</b> agrangian <b>P</b> article <b>T</b> racking
<b>LES</b>	<b>L</b> arge <b>E</b> ddy <b>S</b> imulations
<b>PIV</b>	<b>P</b> article <b>I</b> mage <b>V</b> elocimetry
<b>PLIF</b>	<b>P</b> lanar <b>L</b> aser <b>I</b> nduced <b>F</b> luorescence
<b>PM</b>	<b>P</b> articulate <b>M</b> atter
<b>PNC</b>	<b>P</b> article <b>N</b> umber <b>C</b> oncentration
<b>PTU</b>	<b>P</b> rogrammable <b>T</b> iming <b>U</b> nit
<b>PTV</b>	<b>P</b> article <b>T</b> racking <b>V</b> elocimetry
<b>PVC</b>	<b>P</b> oly <b>V</b> inyl <b>C</b> hloride
<b>QSV</b>	<b>Q</b> uantitative <b>S</b> moke <b>V</b> isualization
<b>RANS</b>	<b>R</b> eynold <b>A</b> veraged <b>N</b> avier <b>S</b> tokes
<b>RMS</b>	<b>R</b> oot <b>M</b> ean <b>S</b> quared
<b>RMSN</b>	<b>R</b> oot <b>M</b> ean <b>S</b> quared <b>N</b> ormalised
<b>ROI</b>	<b>R</b> egion <b>O</b> f <b>I</b> nterest

*Abbreviations*

---

<b>SPM</b>	<b>S</b> uspended <b>P</b> articulate <b>M</b> atter
<b>UFP</b>	<b>U</b> ltra <b>F</b> ine <b>P</b> article
<b>URANS</b>	<b>U</b> nsteady <b>R</b> eynold <b>A</b> veraged <b>N</b> avier <b>S</b> tokes
<b>VFD</b>	<b>V</b> ariable <b>F</b> requency <b>D</b> rive

# Symbols

$h$	Ahmed body height	[ $m$ ]
$b$	Ahmed body width	[ $m$ ]
$C$	Smoke particle concentration	[ppm]
$C_{At}$	Attenuation corrected concentration	[ppm]
$C_G$	Geometric corrected concentration	[ppm]
$C_{ref}$	Reference concentration	[ppm]
$C_{Un}$	Uncorrected concentration	[ppm]
$C_{\dot{Q}}$	Suction parameter	[-]
$d_{md}$	Diameter of mixing duct	[ $m$ ]
$d_s$	Diameter of smoke source	[ $m$ ]
$\mathcal{D}$	Non-dimensional dispersion	[-]
$\delta$	Boundary layer thickness	[ $m$ ]
$\delta_1$	Displacement thickness of boundary layer	[ $m$ ]
$\delta_2$	Momentum thickness of boundary layer	[ $m$ ]
$f$	Focal length of lens	[ $m$ ]
$H$	Typical vehicle height	[ $m$ ]
$H_{cont}$	Height of the wind tunnel test section	[ $m$ ]
$\langle \cdot \rangle$	Time-averaged quantity	[-]
$I, I_e, I_o$	Laser intensity	[-]
$L$	Typical vehicle length	[ $m$ ]
$L_R^*$	Non-dimensional recirculation length	[-]
$L_{cont}$	Length of the wind tunnel contraction section	[ $m$ ]
$L_m$	Mixing length	[ $m$ ]
$l$	Ahmed model length	[ $m$ ]
$\dot{m}_{air}$	Mass flow rate of air	[ $kg/s$ ]
$\dot{m}_{fog}$	Mass flow rate of fog	[ $kg/s$ ]

## Symbols

---

$Q_f$	Volume flow rate of Ethylene Glycol	[ml/s]
$\dot{Q}$	Volume flow rate	[m <sup>3</sup> /s]
$R$	Radius of mixing duct	[m]
$Re_h$	Reynolds number based on model height	[-]
$Re_H$	Reynolds number based on vehicle height	[-]
$Re_l$	Reynolds number based on model length	[-]
$Re_L$	Reynolds number based on vehicle length	[-]
$Re_{lc}$	Critical Reynolds number	[-]
$Re_{\sqrt{FA}}$	Reynolds number based on model frontal area	[-]
$\rho_a$	Density of air	[kg/m <sup>3</sup> ]
$\rho_f$	Density of fog liquid (Ethylene-glycol)	[kg/m <sup>3</sup> ]
$\overline{(\cdot)}$	Spatially-averaged quantity	[-]
$S$	Intensity of scattered light	[-]
$St_p$	Particle Stokes no.	[-]
$\langle T^* \rangle$	Non-dim. mean temp. excess	[-]
$\tau_{flow}$	Characteristic time scale of flow	[s]
$\tau_p$	Particle relaxation time	[s]
$u$	Streamwise velocity	[ms <sup>-1</sup> ]
$u'$	Root-mean-square (RMS) of the fluctuating velocity	[m/s]
$U_\infty$	Free stream velocity	[ms <sup>-1</sup> ]
$\bar{U}_{md}$	average velocity through mixing duct	[ms <sup>-1</sup> ]
$v$	Crossstream verticle velocity	[ms <sup>-1</sup> ]
$\dot{V}$	Volume deficit	[m <sup>3</sup> ]
$W_{belt}$	Width of moving ground/belt	[m]
$W_{model}$	Width of typical vehicle model	[m]
$w$	Crossstream lateral velocity	[ms <sup>-1</sup> ]
$x$	Streamwise distance behind Ahmed body	[m]
$x^*, y^*, z^*$	Non-dimensional lengths	[-]
$\zeta$	Absorption coefficient	[ $\frac{1}{ppm \text{ cm}}$ ]
$z$	Crossstream distance behind Ahmed body	[m]
$\phi$	Angle of rear slant	[°]
$\phi_c$	Critical rear slant angle	[°]
$\overline{\langle C^* \rangle}$	Spatially averaged non-dimensional concentration	[-]
$\mathcal{L}_y$	Vertical dispersion length scale	[-]
$\mathcal{L}_z$	Lateral dispersion length scale	[-]